Self-powered hybrid electromagnetic damper for cable vibration mitigation

Maziar Jamshidi[*1,2], C.C. Chang[1a] and Ali Bakhshi[2b]

[1]*Department of Civil and Environmental Engineering, Hong Kong University of Science and Technology, Hong Kong, China*
[2]*Department of Civil Engineering, Sharif University of Technology, Tehran, Iran*

Abstract.   This paper presents the design and the application of a new self-powered hybrid electromagnetic damper that can harvest energy while mitigating the vibration of a structure. The damper is able to switch between an energy harvesting passive mode and a semi-active mode depending on the amount of energy harvested and stored in the battery. The energy harvested in the passive mode resulting from the suppression of vibration is employed to power up the monitoring and electronic components necessary for the semi-active control. This provides a hybrid control capability that is autonomous in terms of its power requirement. The proposed hybrid circuit design provides two possible options for the semi-active control: without energy harvesting and with energy harvesting. The device mechanism and the circuitry that can drive this self-powered electromagnetic damper are described in this paper. The parameters that determine the device feasible force-velocity region are identified and discussed. The effectiveness of this hybrid damper is evaluated through a numerical simulation study on vibration mitigation of a bridge stay cable under wind excitation. It is demonstrated that the proposed hybrid design outperforms the passive case without external power supply. It is also shown that a broader force range, facilitated by decoupled passive and semi-active modes, can improve the vibration performance of the cable.

Keywords: energy harvesting; vibration control; self-powered damper; bridge cables

1. Introduction

Electromechanical transducers, such as piezoelectric or electromagnetic (EM) instruments are capable of converting mechanical and electrical energy. Due to this capability, such devices are good candidates for use as actuators, sensors and energy harvesters. In the past two decades, many researchers have developed various regenerative control, monitoring and harvesting systems which have found applications in systems such as bridges (Cahill *et al.* 2014, Takeya *et al.* 2016), shock absorbers (Li *et al.* 2013, Shi *et al.* 2014), and structural health monitoring (Casciati and Rossi 2007, Casciati *et al.* 2012). In particular, researchers in industries like automobile and civil engineering have investigated the potential of large scale regenerative vibration control, in order to provide a higher level of harvested power from the vibration (Zuo and Tang 2013). In a typical structural vibration control scheme, the vibrational energy of a structure usually needs to be dissipated to mitigate any excessive vibration. It is thus reasonable to explore whether such dissipated energy can be harvested as electrical energy, which can then be used to power up the needed sensors and processor for the control system.

Among various vibrational energy harvesting techniques, EM devices are more suitable for civil structures, which normally vibrate with low natural frequencies (Green *et al.* 2013). As a vibration harvester, EM devices are often used with a tuned mass damper (TMD) system, with the frequency tuned with the primary frequency of the target structure. These harvesters are usually small scale, and the reactive damping force that they exert on the host structure is negligible. As a vibration control device, such EM devices can be employed in passive, active, and semi-active control system, depending on its configuration. Conventionally, an EM motor is used as an actuator, where it is connected to a servo drive and an external power supply to generate a command force. It is well-known that active devices that benefit from sensor feedback and control algorithms are able to counteract the external disturbance much more effectively. However, the reliance on external power supply has made these active devices potentially unreliable under extreme conditions, such as in hurricanes and earthquakes. On the other hand, passive devices are popular as they are simple, reliable and free from any external power requirement. Semi-active devices have evolved as alternatives having the robustness of passive devices and also the adaptability of active devices. To use the EM device in a semi-active way, an electronic circuit connected to the device is needed to maximize its control performance by regulating the current in the circuit (Scruggs and Iwan 2003). A semi-active device, in contrast to a typical active control one, requires only the power needed for the operation of sensors and microcontrollers. Numerous circuit designs and configurations have been developed that provide both

---

∗Corresponding author, Ph.D. Student
 E-mail: mjamshidi@ust.hk
[a]Professor
 E-mail: cechang@ust.hk
[b]Associate Professor
 E-mail: bakhshi@sharif.edu

damping properties and harvesting capability for larger scale energy harvesting (Ottman *et al.* 2003, Lefeuvre *et al.* 2007). As a result, an EM device can be utilized in a versatile manner and can switch over the different modes of operation conveniently. This is the feature that makes it an ideal candidate for semi-active and hybrid designs.

Compared to other passive or semi-active devices such as magneto-rheological (MR) or viscous dampers, an EM device can incorporate both vibration control and energy harvesting features. This advantage can be exploited to develop the so-called regenerative damper. For instance, Zuo and Cui (2013), Gonzalez-Buelga *et al.* (2015), and Shen *et al.* (2012, 2016) used a dual function EM damper with different energy harvesting circuits for vibration mitigation and energy harvesting in the TMD, where the device was used in a passive form but could be tuned to have the optimal harvesting or vibration mitigation. Shen and Zhu (2015) also studied the application of an EM damper/harvester in a passive configuration to replace viscous dampers for vibration mitigation of stay cables. They described the control performance of passive regenerative damper and the amount of power and energy that could be recovered from the vibration. Some researchers also proposed smart regenerative dampers by attaching an EM harvester with an MR semi-active damper (Cho *et al.* 2005, Choi and Wereley 2009, Jung *et al.* 2011, Chen and Liao 2012), in which the damping properties came mainly from the MR damper rather than the EM harvester.

A sub-class of regenerative dampers is named "self-powered" dampers. They employ the stored energy exclusively to fulfill the power demand of the control force or the intelligent components in the control system. For vehicle suspension systems, researchers developed various kinds of such self-powered shock absorbers (Suda *et al.* 1998, Roshan *et al.* 2015). In the field of civil engineering, researchers incorporated a self-powered semi-active EM damper into a TMD system. Tang and Zuo (2012) proposed circuitry based on an earlier circuit developed by Kim and Okada (2001) to provide variable damping characteristics for such a system. They demonstrated that the feasible force-velocity region of their design was bounded by the properties of the harvesting circuit. Gonzalez-Buelga *et al.* (2014) studied a damper/harvester in a TMD with a variable damping force, and adopted circuitry with a fly-back converter that was capable of a real-time resistance variation. To achieve the desired damping coefficient, the converter must always operate in the discontinuous mode, which casts a restriction on the damping range of the semi-active damper.

In developing a self-powered damper, the energy harvesting circuitry plays a major role. It affects not only the energy harvesting efficiency but also the control performance of the damper. In this paper, a self-powered EM damper with a new circuit design is proposed to study these two aspects. The damper can operate in a hybrid fashion and switch between a passive energy harvesting mode and a semi-active mode, depending on the available energy. Decoupling of these two modes allows the damper to have a better control performance. Moreover, this new design makes the self-power damper more realistic and robust, as the power consumption to support the sensors and microcontrollers is incorporated.

After describing the mechanism of the proposed damper, it's applicability is illustrated for the vibration mitigation of a stay cable in a cable-stayed bridge. Owing to their high flexibility and low inherent damping, stay cables are susceptible to excessive vibration caused by the ambient disturbance like wind (Main *et al.* 2001). Through the numerical simulations, the advantage of the proposed damper is evaluated when it is compared with the alternative control approaches.

2. Mechanism of self-powered hybrid EM damper

The main components of the proposed self-powered hybrid EM damper are illustrated in Fig. 1 where the damper is attached to a structural system at point *d*. In this configuration, the linear velocity *v* induced at point *d* under some external disturbance is mechanically converted to rotational motion by a linear-to-rotational conversion mechanism like a ballscrew or leadscrew. This causes the motor's rotor to rotate at an angular velocity *ω*. In this study, the motor is assumed to be a rotary three-phase AC permanent magnet synchronous motor. Comparing to a linear motor or a rotary DC machine, AC synchronous motors have a lower coil resistance and are able to generate larger back electromotive force (back-emf) under a given input velocity. This makes them a perfect choice for energy harvesting purpose (Cassidy *et al.* 2011). According to Faraday's law of induction, the angular velocity of the rotor relative to the stator *ω* creates a back-emf *e* in each phase of the motor. This internal voltage, depending on the circuit attached to the terminals of the motor, causes current *i* to flow inside the circuit and coils. According to Lorentz law, this current produces a reactive torque *T* to counteract the motion in the presence of a magnetic field. Subsequently the resistive torque *T* is converted to a linear force f_{em} at the point of attachment *d* in the opposite direction to the linear velocity *v*. Each of the three coils of the stator in the rotary motor, called phases, has its own back-emf *e*, coil resistance *r* and inductance L_c. Using the Park transformation, the electrical circuit can be approximated to an equivalent circuit with the following electrical and mechanical relationship (Pillary and Krishnan 1989, Cassidy *et al.* 2011, Cassidy 2012),

$$e = \frac{3}{2} k_e \cdot \omega \qquad (1)$$

$$T = \frac{3}{2} k_e \cdot i \qquad (2)$$

where k_e is a rotary motor constant. Assuming that the conversion between the linear and rotational motion has no losses and can be related linearly by a conversion factor η, then
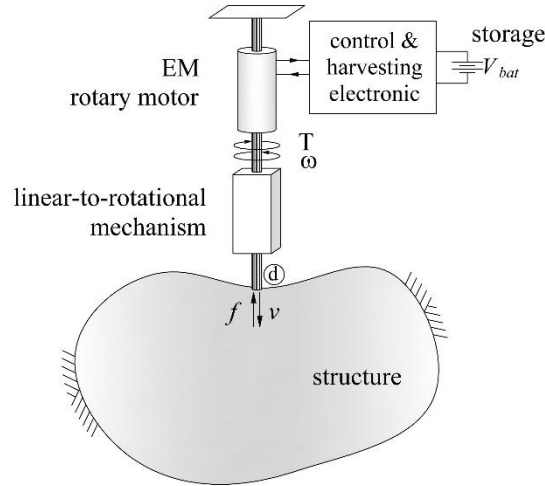
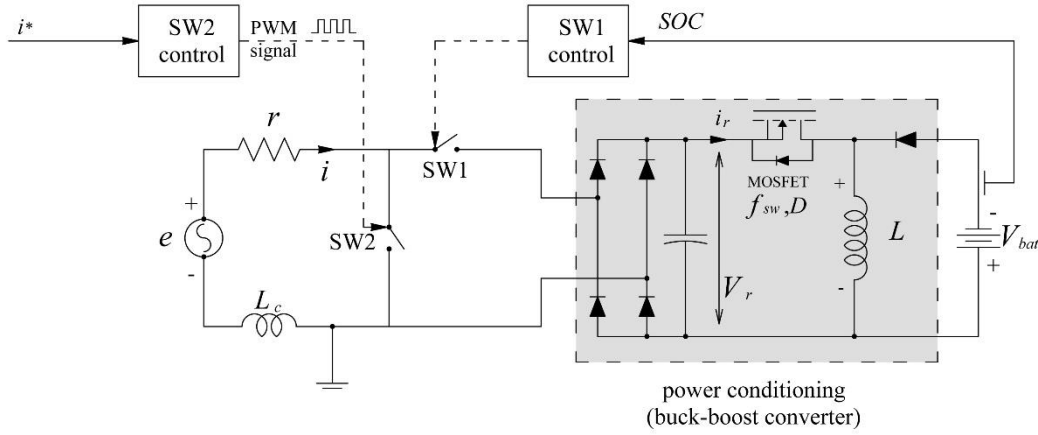Fig. 1 Schematic diagram of the main components of the device

Fig. 2 Proposed hybrid control circuitry

$$\omega = \eta \cdot v \qquad (3)$$

$$T = \frac{f_{em}}{\eta} \qquad (4)$$

Substituting Eqs. (3) and (4) into Eqs. (1) and (2), respectively, the dynamic equations of EM damper in terms of linear quantities becomes

$$e = k_v v \qquad (5)$$

$$f_{em} = k_v \cdot i \qquad (6)$$

where the linear motor constant k_v is

$$k_v = \frac{3}{2} \eta \cdot k_e \qquad (7)$$

The relationship between i and e, however, is determined by the circuit used in the damper. Depending on the topology of the circuit, the force-velocity governing the characteristics of damper can be established. In addition to the electromechanical force (f_{em}), the motor and linear-to-rotational convention system produces additional friction and parasitic damping force (Shen and Zhu 2015). Thus, the total force exerted on the structure can be expressed as

$$f = f_{em} + c_d v + f_c . \text{sgn}(v) \qquad (8)$$

where c_d and f_c are the parasitic damping coefficient and the friction force of the damper, respectively.

Fig. 2 displays a circuit that can realize the desired hybrid feature for the damper proposed. The circuit contains power conditioning electronics incorporated with a buck-boost DC-DC converter (Lefeuvre *et al.* 2007, Shen and Zhu 2015) and two switches "SW1" and "SW2" to control the mode of operation for the damper. The damper can alternate between the passive mode and the semi-active mode.

In the passive mode, the electrical energy converted from the vibrational energy is accumulated in a rechargeable battery through the harvesting circuit. When sufficient energy is accumulated in the battery, the damper is switched to the semi-active mode and continues to operate in this mode as long as the battery energy level is

above a threshold that can sustain this semi-active operation. Otherwise, the damper goes back to the passive mode and begins to harvest energy again.

2.1 Passive mode

In the passive mode (with SW1="on"; SW2="off"), the EM motor is directly connected to a rechargeable battery through the cascade of a full-bridge rectifier and a buck-boost DC-DC converter. The function of the buck-boost DC-DC converter is in regulation by stepping up or down the output power. The key component of this converter is a metal-oxide-semiconductor field-effect transistor (MOSFET) switch, which turns on and off with high frequency and magnetizes or demagnetizes the inductor L. The switch is fed by a pulse-width modulation (PWM) signal at a given frequency f_{sw} and a duty cycle D. Lefeuvre *et al*. (2007) showed that for a given f_{sw}, the duty cycle D (between 0 to 1) can be selected such that the converter simulates a desired resistance, with a major difference that the electrical power is stored in the battery instead of being dissipated through heat. The equivalent resistance of the converter R_0 can be obtained as

$$R_0 = \frac{2Lf_{sw}}{D^2} \qquad (9)$$

Note that this equation is valid as long as the converter operates in the so-called discontinuous condition mode (DCM). This is guaranteed if the duty cycle D is set to a value that satisfies the following inequality (Lefeuvre *et al*. 2007)

$$D < \frac{1}{1 + V_r/V_{bat}} \qquad (10)$$

where V_r and V_{bat} are the input voltages to the buck-boost converter and the voltage of the rechargeable battery, respectively (Fig. 2). By estimating the maximum input voltage, D can be selected such that the buck-boost converter operates in the DCM. Replacing the harvester circuit with its equivalent resistance R_0, the dynamic behavior of circuit can be described as

$$e = (r + R_0)i + L_c \frac{di}{dt} \qquad (11)$$

where r and L_c are the coil resistance and inductance, respectively. Because of the low variation of current, which is a typical result for application to civil engineering structures with low vibration frequencies (below 10 Hz), and small value of inductance L_c, the effect of coil inductance in the last term can be neglected and Eq. (11) can be simplified as (Zhu *et al*. 2012)

$$i = \frac{e}{r + R_0} \qquad (12)$$

Substituting Eq. (12) into Eq. (6) and incorporating Eq. (5), the force-velocity relationship can be established as

$$f = \frac{k_v^2}{r + R_0} v \qquad (13)$$

This equation is analogous to the characteristic equation of a linear viscous damper with the damping coefficient c_0 equals to

$$c_0 = \frac{f}{v} = \frac{k_v^2}{r + R_0} \qquad (14)$$

There are various circuit designs for harvesters that can provide favorable resistive behavior, however each has its own limitation and range of operation. Buck-boost converter, which is used in this study, is a popular DC-DC converter that can be used for this purpose (Shen and Zhu 2015). The power input into the battery P_{bat} under this passive mode can be estimated as

$$P_{bat} = \eta_e R_0 i^2 \qquad (15)$$

where η_e is the electrical efficiency of the buck-boost converter to account for the power loss present in the circuit.

2.2 Semi-active mode

Referring to Fig. 2, the switch SW2 helps to realize the semi-active function of the damper. A PWM signal with a fixed frequency and a duty cycle δ (varying between 0 and 1) determines the state of SW2. The switching frequency is typically higher than the frequency content of the input voltage derived from the vibration. Hence the input voltage e can be considered constant during each switching period $T_{sw,2}$. Since the switching action happens very quickly, the current can be varied by changing the duration of switch "on" mode in each duty cycle.

Depending on the state of SW1, two cases for the semi-active mode described below are possible.

2.2.1 Case (a): Non-energy harvesting semi-active

In this case, the energy harvesting electronics section is disconnected from the rest of the circuit (SW1="off"). Fig. 3 demonstrates the current and voltage waveforms for SW2, which acts in the manner of a chopper. As shown in Fig. 3, no current passes through the circuit when SW2 is off. Once SW2 is "on", a maximum current of e/r flows in the circuit.

The average current during a switching period is given by

$$i = \frac{\delta}{r} e \qquad (16)$$

This shows that the circuit exhibits an equivalent resistance that can be tuned in accordance with the duty cycle of PWM. However, it should be ensured that the switching period $T_{sw,2}$ is longer than the time constant of the coil ($\tau = L_c/r$) in such a way that the current passes the transient state fast enough. This will be further explained in details in Section 3.4.1.

The equivalent resistance R_{eq} and its corresponding damping coefficient C_{eq} are given as
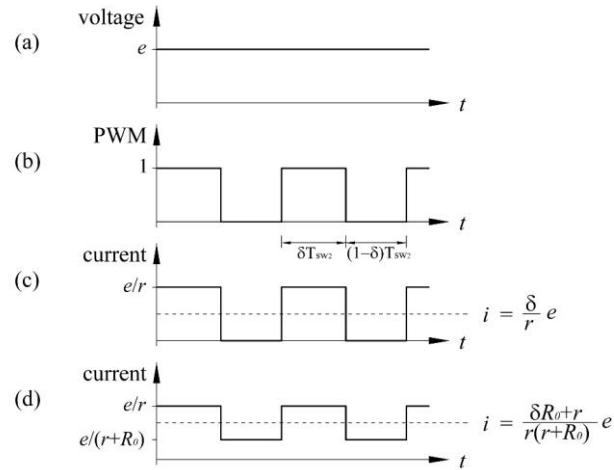
Fig. 3 (a) Voltage, (b) PWM signal, (c) Current waveform of SW2 (Case (a)) and (d) Current waveform of SW2 (Case (b))
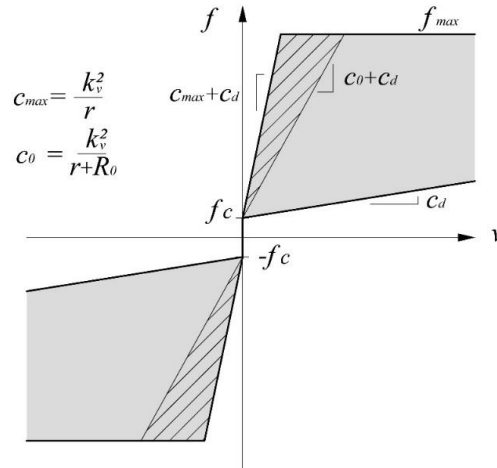

Fig. 4 Feasible force-velocity region

$$R_{eq} = \frac{r}{\delta} \tag{17}$$

$$C_{eq} = \frac{k_v^2}{r}\delta \tag{18}$$

By adjusting the duty cycle of SW2 (δ) between 0 and 1, the electromechanical damping of the device can be adjusted in real time between 0 and k_v^2/r.

The gray area in Fig. 4 shows the feasible operation region of force-velocity that the damper can provide under this case. The boundaries of the feasible force region are prescribed by the properties of the rotary motor which determines the maximum damping and force magnitude that the damper can produce. Note that the maximum force f_{max} is related to the stall torque of the motor T_{stall}. The battery power P_{bat} in this case is negative and is equal to the power consumption of the monitoring and processing unit P_0,

$$P_{bat} = -P_0 \tag{19}$$

Note that the disconnection of SW1 in this case enables the damper to have a wide range of damping coefficient which can be seen when compared to the following case.

2.2.2 Case (b): Energy harvesting semi-active

An alternative approach is to keep SW1 connected during the semi-active mode, hence the circuit can continue to harvest energy. A similar concept was adopted by Tang and Zuo (2012) for a regenerative semi-active damper. Following the approach described above, the average current i in this case can be obtained as below (see Fig. 3(d))

$$i = \frac{r + \delta R_0}{r(r + R_0)}e \tag{20}$$
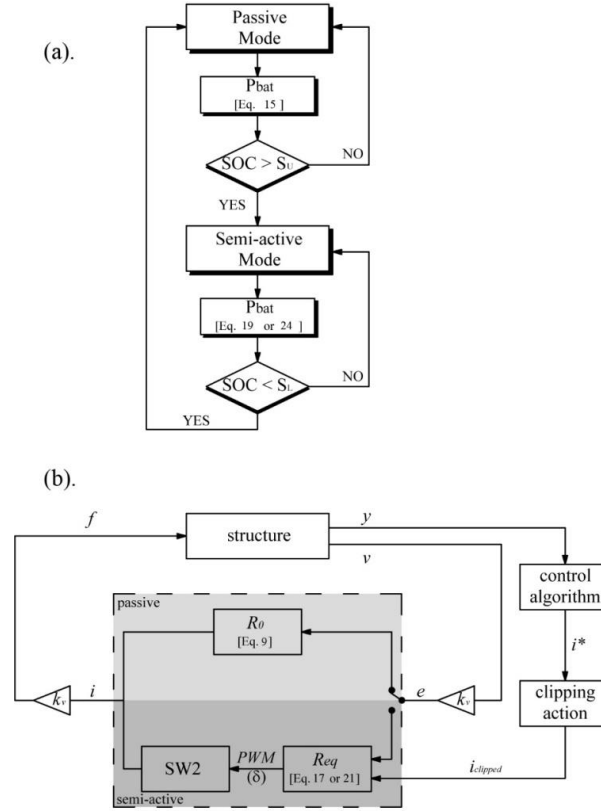
The equivalent resistance and damping are given as

Fig. 5 Flowchart of switching between two modes (a), and hybrid control block diagram (b)

$$R_{eq} = \frac{r(r+R_0)}{r+\delta R_0} \qquad (21)$$

$$C_{eq} = k_v^2 \frac{r+\delta R_0}{r(r+R_0)} \qquad (22)$$

Again, by adjusting the duty cycle of SW2 (δ) between 0 and 1, the electromechanical damping of the device can be adjusted in real time between $k_v^2/(r+R_0)$ and k_v^2/r as shown in the hatched area in Fig. 4. It can be seen that comparing to Case (a), where SW1 is disconnected, the feasible force region of the damper for Case (b) is smaller, although Case (b) is able to harvest energy while performing semi-active control. The instantaneous harvested power (P_{har}) flowing into the battery is

$$P_{har} = \begin{cases} 0 & \text{SW2: on} \\ \eta_e R_0 \dfrac{e^2}{(r+R_0)^2} & \text{SW2: off} \end{cases} \qquad (23)$$

Substituting e from Eq. (20), into (23), the average power to the battery (P_{bat}) during each switching cycle can be obtained as

$$P_{bat} = \frac{(1-\delta)r^2}{(r+\delta R_0)^2} \eta_e R_0 i^2 - P_0 \qquad (24)$$

2.3 Hybrid operation

In principle, the damper can always operate in the semi-active mode when the battery power is larger than the power required to operate the semi-active mode. If this is not the case, switching between the semi-active mode and the passive mode is necessary when the battery cannot maintain its constant output voltage V_{bat} due to the energy depletion. For example, the battery voltage for an NiMH battery drops below its nominal voltage when its state-of-charge (SOC) drops below 20% (Tremblay and Dessaint 2009). Hence an SOC of 20% can be used as a threshold S_L for switching the damper from the semi-active mode to the passive mode. To switch from the passive mode back to the semi-active mode, it is suggested that a higher SOC value S_U, say 30%, be used to avoid rapid alternation between modes. Such an undesirable chattering effect can be harmful to sensors, processors, and the power electronics (Sarkar 2015). This upper bound parameter is a flexible value, which could depend on the battery capacity, power demand (P_0), and the duration of excitation. The higher this value is the longer it takes for the battery to charge-up and switch to the semi-active mode, and it stays longer in this mode as well. Hence, it is possible that the damper could remain in the passive mode for the whole time if the duration of excitation is not long enough. Fig. 5(a) shows the operation flowchart of the proposed hybrid damper.

Assuming that the initial SOC of the battery is zero, the damper will operate in the passive mode and harvest energy continuously until the battery SOC exceeds S_U. The damper will be switched to the semi-active mode and remain in this mode as long as the battery SOC is above the lower level S_L.
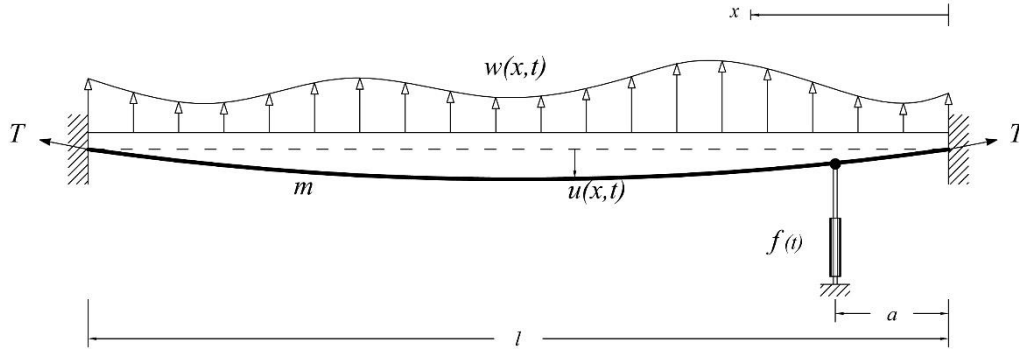
Fig. 6 Cable equipped with the EM hybrid damper

As explained above, there are two possible operations for the semi-active mode: non-energy harvesting and energy harvesting, by keeping SW1 "off" or "on", respectively. These operations have their own advantages and disadvantages which need to be validated and are explained in the numerical study.

Fig. 5(b) further shows the block diagram of the damper-structure system. In the passive mode, the damper properties are constant which results in an equivalent damping coefficient (Eq. (14)) for the structure. While in the semi-active mode, the current calculated from an optimal control algorithm is clipped according to the feasible force region of the damper. The clipped current and the back-emf e are then used to determine the equivalent resistance of the circuit and the duty-cycle of the signal feeding into the switch SW2. While most other designs assume that adequate energy can always be harvested at any time instant to power up the semi-active mode, the proposed hybrid operation can quantitatively and realistically consider the power demand for the semi-active control of the damper and the amount of energy that can be harvested by the damper.

3. Application to cable vibration control

In this section, the proposed self-powered hybrid EM damper employed to reduce the vibration of stay cables under wind excitation is described.

3.1 System model

Application of deck-anchored dampers is a common measure for suppression of the unfavorable cable vibrations (Pacheco *et al.* 1993, Yu and Xu 1998, Krenk 2000, Main and Jones 2001, Zhou *et al.* 2006, Johnson *et al.* 2007, Huang *et al.* 2012). Assume that a cable of length l is equipped with a self-powered hybrid EM damper at a distance a from the support (see Fig. 6). The cable is assumed to have a small-sag-to-span ratio (around 1% (Johnson 2007)), hence the effect of the initial gravitational static deflection and inclination can be ignored (Irvine 1981). Modeling this cable as a taut string, its equation of motion can be written as

$$m\frac{\partial^2 u}{\partial t^2} + c\frac{\partial u}{\partial t} - T\frac{\partial^2 u}{\partial x^2} = w(x,t) + f(t) \cdot \delta(x-a) \quad (25)$$

Where u is the in-plane transverse displacement, m and c are mass and damping per unit length of the cable, respectively, T is the axial constant tension force along the cable, w is the distributed lateral external load, f is the force imposed from the damper, and x is the coordinate along the axial direction of the cable. The vector of the mode shapes of a taut cable has a sinusoidal form of

$$\mathbf{\Phi}(x) = \left[\sin\left(\frac{i\pi x}{l}\right)\right]_{n\times 1} \qquad i=1,2,\cdots n \qquad (26)$$

where $\mathbf{\Phi}(x)$ is the vector of the mode shape amplitudes at the location x and n = number of modes. Therefore the state-space representation of cable-damper system can be presented in modal coordinates as follows

$$\begin{Bmatrix}\ddot{\mathbf{q}}\\\dot{\mathbf{q}}\end{Bmatrix} = \begin{bmatrix}-2\mathbf{\Omega}\mathbf{Z} & -\mathbf{\Omega}^2\\\mathbf{I} & \mathbf{0}\end{bmatrix}\begin{Bmatrix}\dot{\mathbf{q}}\\\mathbf{q}\end{Bmatrix} + \begin{Bmatrix}\mathbf{M}^{*^{-1}}\mathbf{\Phi}(a)\\\mathbf{0}\end{Bmatrix}f + \begin{Bmatrix}\mathbf{M}^{*^{-1}}\mathbf{w}^*\\\mathbf{0}\end{Bmatrix} \quad (27)$$

where $\ddot{\mathbf{q}}$, $\dot{\mathbf{q}}$ and $\mathbf{q}$ are the modal acceleration, velocity and displacement vectors, respectively; $\mathbf{\Omega}$, $\mathbf{Z}$, $\mathbf{M}^*$ and $\mathbf{w}^*$ are the matrices for natural frequency, damping ratio, modal mass and modal force and can be expressed respectively as

$$\mathbf{\Omega} = \left[\frac{i\pi}{l}\sqrt{\frac{T}{m}}\delta_{ij}\right]_{n\times n} \qquad i,j=1,2,\cdots n \qquad (28)$$

$$\mathbf{Z} = \left[\xi_i\delta_{ij}\right]_{n\times n} \qquad i,j=1,2,\cdots n \qquad (29)$$

$$\mathbf{M}^* = \left[\frac{ml}{2}\delta_{ij}\right]_{n\times n} \qquad i,j=1,2,\cdots n \qquad (30)$$

$$\mathbf{w}^* = \left[\int_0^l w(x,t)\sin\left(\frac{i\pi x}{l}\right)dx\right]_{n\times 1} \qquad i=1,2,\cdots n \quad (31)$$

where ξ_i is the ith mode damping ratio and δ_{ij} is the Kronecker delta.
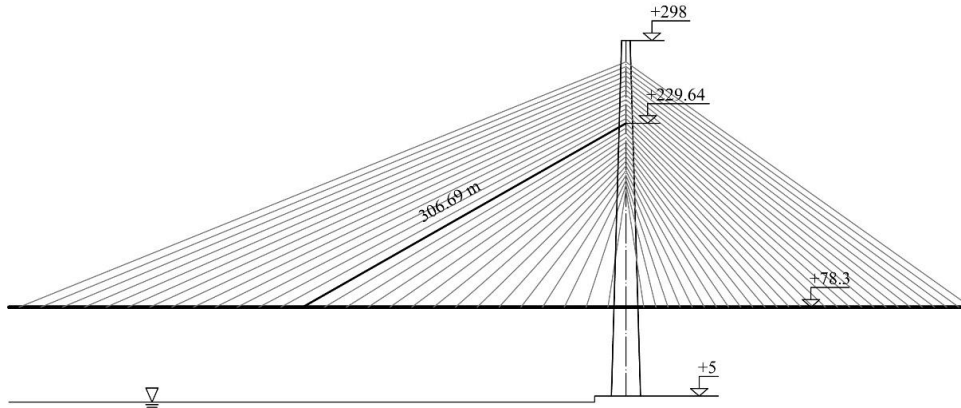
Fig. 7 Elevation of Stonecutters bridge and the stay cable used in the modeling

3.2 Cable and wind parameters

For this numerical simulation, the properties of cable from one of the stay cables of the Stonecutters Bridge in Hong Kong were used (Shen and Zhu 2015): l=306.69 m, m=98.6 kg/m, T=5.53 MN, and ξ_1=0.5%. The schematic illustration of the stay cable is presented in Fig. 7. The first natural frequency of the cable was 0.385 Hz and the damper location a=0.03l. The first 20 modes of the cable were considered in the simulation. There are a number of mechanisms that may cause a stay cable to vibrate under the action of wind flow, including buffeting, vortex shedding, galloping and rain-wind induced vibration (Caetano 2007).

For illustrative purposes, it was assumed that the cable was under random buffeting wind excitation (Hui *et al.* 2009a, Hui *et al.* 2009b), and synthesized using the von Kármán spectra model (von Kármán 1948) following the parameters given in (Shen and Zhu 2015) and (Hui *et al.* 2009a) for the site of Stonecutters bridge. The variation of mean wind speed with height followed the power law with an exponent equal to 0.29, and the turbulence intensity used to find the standard deviation of the turbulence component was 0.235. It was further assumed that the cross-power spectral density had a bandwidth of 0-8 Hz which could excite all first 20 modes of the cable. In order to numerically evaluate the modal wind force in Eq. (31), discretized along wind buffeting velocity time histories were generated for 40 equally spaced nodes across the cable.

Table 1 Cable Properties (Stonecutters Bridge, Hong Kong)

Property	Value
Cable length [m]; l	306.69
Mass [kg/m]; m	98.6
Horizontal tension force [kN]; T	5529.6
Natural frequency [rad/sec]; ω_0	2.42
First mode damping ratio; ξ_0	0.005
Damper location; a/l	0.03
Inclination [°]; α	19.23
Cable diameter [m]; d_0	0.15
Wind drag coefficient; C_D	1.15

At the kth node the total wind speed was the summation of the mean wind speed $\bar{v}_k$, which was a function of height, plus a turbulence component v'_k

$$v_k(t) = \bar{v}_k + v'_k(t) \tag{32}$$

The discrete along wind drag force $\tilde{w}_k$ is then obtained by

$$\tilde{w}_k(t) = \frac{1}{2} C_D \rho_{air} d_0 v_k^2(t) \tag{33}$$

where C_D, d_0 and ρ_{air} are the cable's drag coefficient, cable diameter, and air density, respectively. Please see Table 1 for a summary of parameters used in the simulation. In the following, the mean wind speed is referred to the 10-minute mean wind speed at a 10-m height above the sea level.

3.3 Control system design

3.3.1 Semi-active control

For semi-active control, a clipped optimal algorithm was used (Dyke *et al.* 1996, Johnson *et al.* 2007). In this strategy, the control force $f^*(t)$ was calculated according to an active optimal control law and was clipped based on the damper's feasible region as shown in Fig. 4. For the active control law, a linear quadratic regulator (LQR) algorithm was employed as the state feedback controller. The main priority here is to minimize the mean square of displacement response across the cable, as defined below (Johnson *et al.* 2007),

$$\sigma_{disp}^2 = E\left[\int_0^l u^2(x,t)dx\right] = \frac{1}{m}E\left[\mathbf{q}^T\mathbf{M}^*\mathbf{q}\right] \tag{34}$$

Thus the objective function for the LQR control is defined as

$$J = \lim_{T\to\infty} E\left[\frac{1}{T}\int_0^T \left(\mathbf{q}^T\mathbf{M}^*\mathbf{q} + Rf^2\right)dt\right] \tag{35}$$

where R is a weighting coefficient governing the weighting

between response reduction and control effort. In this study, it was assumed that $R = 5 \times 10^{-8}$ m·s²/N which resulted in the first modal damping ratio of 0.24 for the closed-loop system. The feedback control force, therefore can be calculated as below

$$f^* = -\mathbf{G} \cdot \begin{Bmatrix} \dot{\mathbf{q}} \\ \mathbf{q} \end{Bmatrix} \tag{36}$$

where **G** is the gain matrix obtained from the solution of the algebraic Riccati equation. Referring to Eqs. (32) and (33), it could be expected that the steady-state displacement of the cable under this type of loading would be non-zero.

However the main control objective is to mitigate the fluctuating vibration. Thus, the displacement state vector in the objective function as shown in Eq. (35) is replaced by the fluctuating displacement vector.

3.3.2 Passive control

For the passive case, the optimal damping coefficient for the first mode of cable is used as (Pacheco *et al.* 1993)

$$c_{opt} = 0.1 \frac{m l \omega_{o1}}{a/l} \tag{37}$$

where ω_{01} is the first natural frequency of the cable. Equating Eq. (37) to (14), the equivalent emulated resistance R_0 can be obtained. According to Eq. (37) the optimal damping coefficient for the given cable and damper's location was found to be 244.52 kN-sec/m.

3.4 Damper parameters

A wide range of choices are available for the EM motor. It is clear that motors with higher capacity, i.e., larger motor constant and saturation force but smaller internal resistance and coil inductance, are more suitable for mitigating cable vibration. For this numerical analysis, the Kollmorgen AKM42E (Kollmorgen 2016) three-phase permanent-magnet synchronous motor was adopted. Also, an EC3 ballscrew driven by 4 mm leads was used for the linear-to-rotational conversion. The properties of the EM damper are summarized in Table 2. A realization of such an EM damper plus a linear-to-rotational conversion mechanism has been provided by Cassidy (2011) and is redrawn here for clarity.

The properties of the electrical components for the passive mode and the semi-active mode are given in Tables 3 and 4, respectively. For the buck-boost converter, the inductance L was equal to 12.25 μH, the MOSFET switching frequency f_{sw} was 1 kHz, and the duty cycle was set to 5% to ensure that the converter operated in the DCM. The emulated resistance of the converter in this case was equal to 9.8 Ω, which together with the coil resistance (2.41 Ω) and the estimated parasitic resistance (1.30 Ω) produced 13.51 Ω resistance. An NiMH rechargeable battery with a voltage of 9.6 V and the rated capacity of 150 mAh was used as the storage element. The power consumption of an Imote2 sensor during the active sensing

mode was approximately 620 mW (Shen *et al.* 2016). Considering the number of sensors needed at different locations to monitor the cable's vibration, along with the power demand for the microcontrollers, P_0=10 W was selected as a preliminary estimate for the power consumption to support the semi-active operation. Further investigations might be necessary to have a more accurate estimation. The initial SOC of the battery was assumed to be 20% and the thresholds for switching between the semi-active mode and the passive mode were set at 20 and 30% for S_L and S_U, respectively. Two hybrid cases were simulated: Case (a): energy harvesting passive and non-energy harvesting semi-active; and Case (b): energy harvesting passive and energy harvesting semi-active.

Table 2 EM motor properties (based on the EC3 ballscrew and AKM42E motor (KOLLMORGEN))

Property	Value
Rotary motor constant [N.m/A]; k_e	0.77
Linear motor constant [N/A]; k_v	1814
Coil resistance [Ω]; r	2.41
Coil inductance [mH]; L	8.93
Ballscrew lead [mm/rev]; $2\pi/\eta$	4
Torque at stall [N.m]; T_{stall}	9.74
Maximum force [kN]; f_{max}	15.3
Maximum damping coefficient [kN.sec/m]; c_{max}	1365
Parasitic damping coefficient [N.sec/m]; c_d	951
Friction force [kN]; f_c	98.9

Table 3 Electrical circuit properties of the passive mode

Property	Value
Inductor [μH]; L	12.25
Inductor resistance [mΩ]; R_L	30
Bridge filter capacitor [μF]; C_1	470
Capacitor resistance [mΩ]; R_{C1}	40
Battery filter capacitor [μF]; C_2	220
Capacitor resistance [mΩ]; R_{C2}	65
Diode forward voltage [V]; V_f	0.5
MOSFET drain-source on-resistance [mΩ]; $R_{DS(on)}$	60
MOSFET switching frequency [Hz]; f_{sw}	1000
MOSFET switching duty-cycle [%]; D	5
Battery voltage [V]; V_{bat}	9.6
Battery rated capacity [mAh]	150
Estimated parasitic resistance [mΩ]	1.30

Table 4 Electrical circuit properties of the semi-active mode

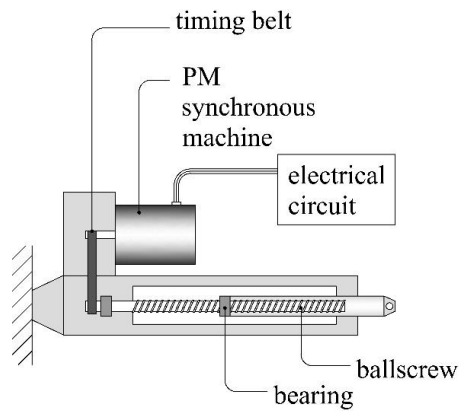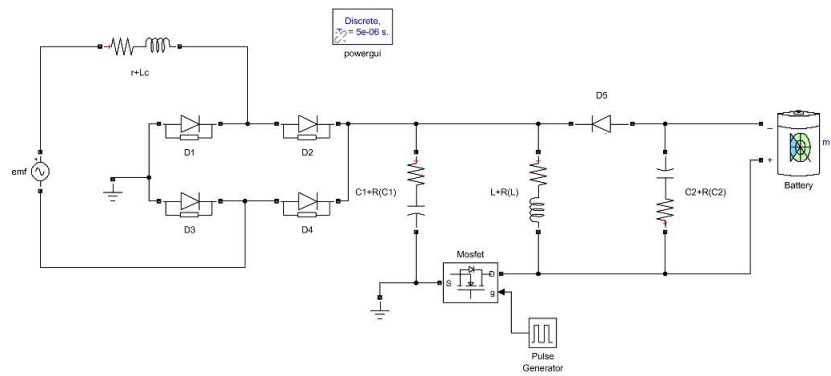| Property	Value
MOSFET switching frequency [Hz]; f_{sw2}	20
Minimum duty cycle [%]; δ_{min}	20
Maximum duty cycle [%]; δ_{max}	100
Switch series added resistance [Ω]; R_{sw2}	5
Parasitic resistance of the circuit [Ω]	0.25
Minimum EM damping coefficient [kN.s/m]	85.92
Maximum EM damping coefficient [kN.s/m]	429.58

Fig. 8 Schematic view of the EM motor and linear-to-rotational system (Cassidy *et al.* (2011))

(a)
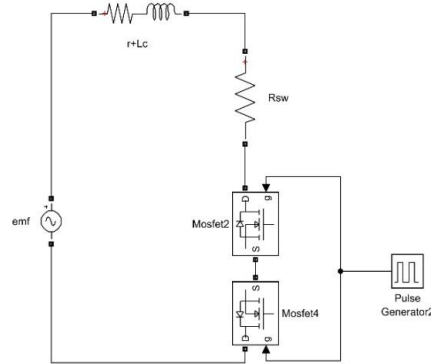
(b)

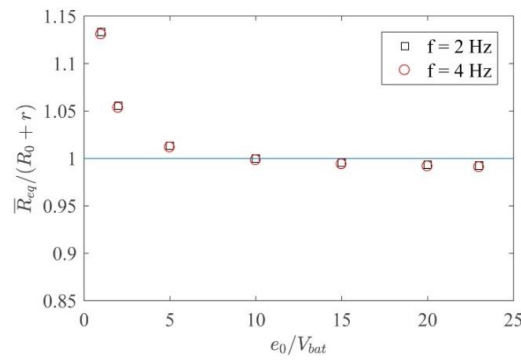Fig. 9 Simulink models of the (a) passive, and (b) semi-active circuits

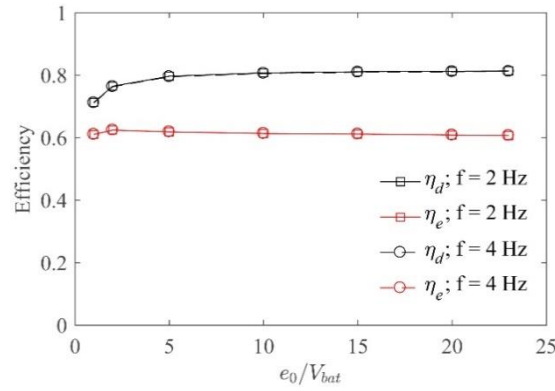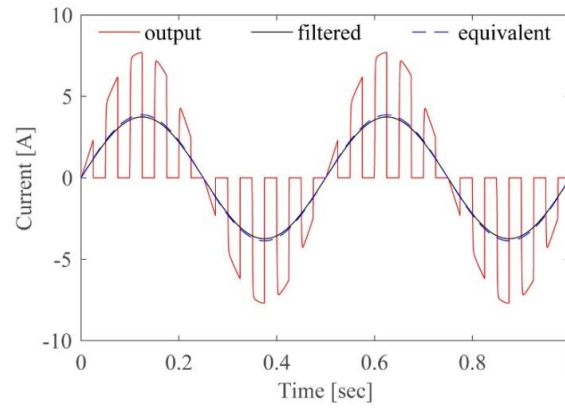Fig. 10 Equivalent resistance of the circuit in passive mode

Fig. 11 Efficiency of the harvesting circuit in passive mode

Fig. 12 Comparison of the actual output current with theory ($e_0/V_{bat} = 10, f = 2$ Hz)

3.4.1 Numerical evalutation of the circuit

In this section, the behavior of the circuits is investigated under harmonic AC input voltage with the amplitude and frequency of e_0 and f. Figs. 9(a) and 9(b) illustrate the Simulink models of the circuit for the passive mode and the semi-active mode, respectively. Fig. 10 shows the average equivalent actual resistance over the required resistance of the circuit versus the normalized input voltage over the battery voltage. It can be observed that for the input voltage above $5V_{bat}$ the circuit can emulate the designed resistance with a good accuracy. The increase in resistance for the lower input voltages can be attributed to the voltage dope ($2V_f$) across the bridge rectifier for lower input voltages. For the present study, the range of generated back-emf due to the velocity of the cable is much higher that $5V_{bat}$, hence it is reasonable to assume a desired constant resistance of 13.51 Ω.

Two efficiency ratios η_d and η_e are defined as

$$\eta_d = \frac{\int V_r(t).i_r(t)dt}{\int e(t).i(t)dt} \tag{38}$$

$$\eta_e = \frac{\int V_{bat}(t).i_{bat}(t)dt}{\int V_r(t).i_r(t)dt} \tag{39}$$

where η_d reflects the power loss in the coil and bridge rectifier and η_e is a measure of power loss in the buck-boost converter. Fig. 11 demonstrates these efficiency factors with respect to the normalized input voltage. It is seen that the efficiency of the buck-boost converter (η_e) can be estimated as 0.61. For the coil efficiency (η_d), theoretically, by substituting the buck-boost converter with its equivalent resistance in the circuit η_d can be estimated as 0.82, which is consistent with the results shown in Fig. 11.

In the semi-active mode, as a result of high switching frequency occurring in the circuit, the inductance of coil (L_c) cannot be ignored. It needs to be considered when determining the minimum damping coefficient of the damper. In order word, the switching frequency should be small enough such that the duration of switch "on" ($\delta T_{sw,2}$) is longer than the time constant ($\tau=L_c/r$) of the circuit. In this way, during the time that SW2 is closed, it sustains the maximum current for a larger portion of time.

To reduce the time constant of the circuit to an acceptable range (1.16 milliseconds), a resistor ($R_{sw}=5\Omega$) (see Fig. 9(b)) is connected in series with SW2. It must be noted that the added resistance would reduce the maximum damping available to the damper. Based on the time constant of coil, a suggested upper bound for switching frequency can be given as
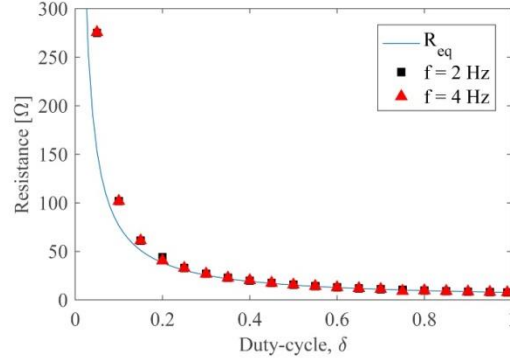
Fig. 13 Variation of the average circuit resistance with duty cycle in semi-active mode
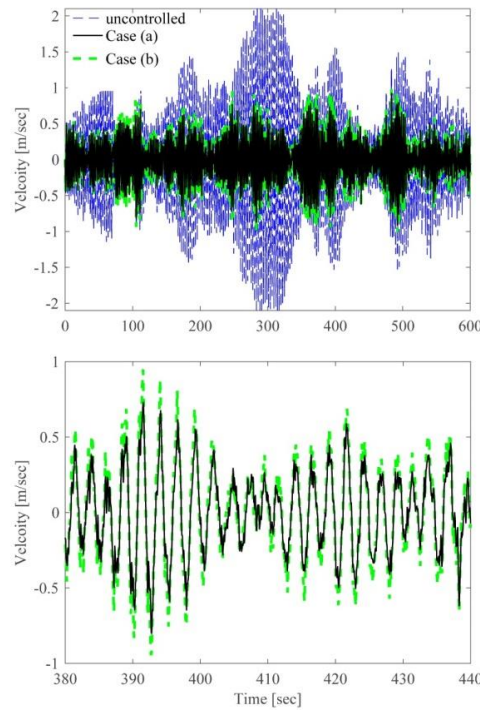

Fig. 14 Mid-point velocity of cable (mean wind speed = 17 m/sec): (a) 0-600 sec, and (b) 380-440 sec

$$f_{sw,2} < \delta_{min} \frac{(r + R_{sw})}{4L_c} \qquad (40)$$

For the switching frequency of 20 Hz and δ=0.5, the time history of the output current is plotted in Fig. 12. It can be seen that the resulting filtered current matches well with the equivalent theoretical values. Fig. 13 shows the values of the circuit average output resistance under different values of duty cycle. It is seen that the emulated resistance agrees well with the theoretical value for duty cycle above 0.2. Hence, this value was used as δ_{min}, to determine c_{min} of the semi-active mode.

3.5 Simulations results of the stay cable

After the characteristics of the hybrid EM damper have been verified and the efficiency of the electrical circuit have been found, the electrical circuits are replaced by the force-velocity relationship derived earlier to allow a larger time step of 0.001 seconds for more efficient computation. Fig. 14(a) shows the response of the mid-point of the cable under a mean wind speed of 17 m/s for 600 seconds of wind excitation. Velocity of unimpeded cable with no damper was compared to the hybrid Case (a) and Case (b). It can be seen that the response of hybrid design, for both cases has been improved with no external power demand. To display the advantage of Case (a) over Case (b), a 60-second duration of velocity time history is also illustrated in Fig. 14(b). Fig. 15 shows the damper force versus velocity at the attachment point of the cable. It can be seen that the feasible regions in which the damper was able to function are compatible with those shown in Fig. 4. Fig. 15 shows that the force-velocity region of Case (b) only covers a small portion of the region that Case (a) is able to provide.
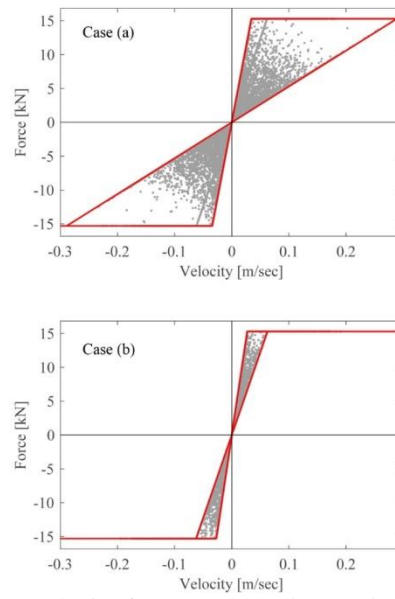
Fig. 15 Damper force versus velocity for Case (a) and Case (b) (mean wind speed = 17 m/sec)
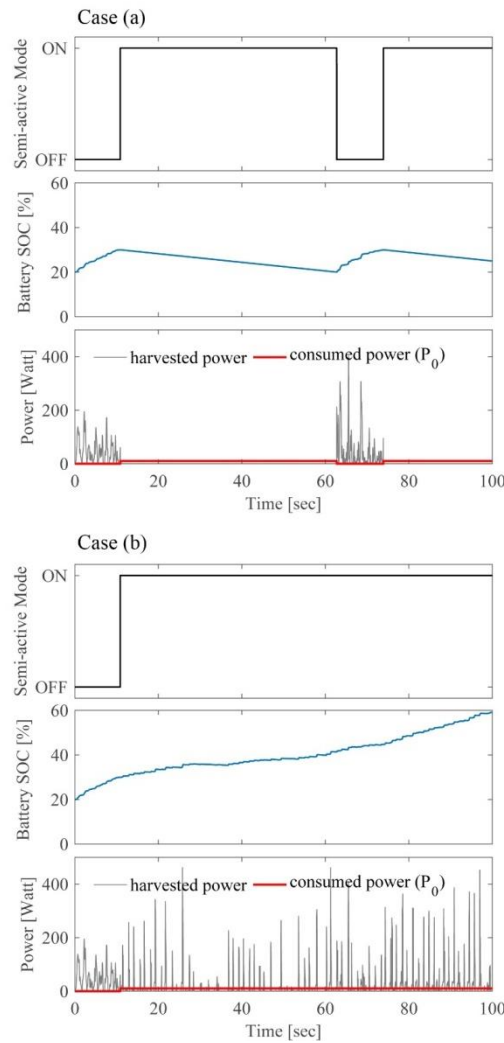

Fig. 16   Semi-active state, battery state-of-charge (SOC) and power flow time history for Case (a) and Case (b) (mean wind speed = 17 m/sec)

Figs. 16(a) and 16(b) demonstrate the operation of the damper for Case (a) and Case (b), respectively. The upper figures show the operational mode of the damper at each time step, and the middle ones display the time-history of the battery SOC. The harvested power and power consumption are also plotted in the lower figures. In these figures, the harvested power is the net power that flows into the battery at each time instance. In Case (a), during the time that semi-active mode is "on", no power is harvested, while in Case (b) the excess power is permitted to flow into the battery.

3.6 Comparison with other control strategies

To demonstrate the performance of this new hybrid control approach, the RMS's of the displacement response σ_d and velocity response σ_d of the cable were used as performance indices and were calculated respectively as

$$\sigma_d = \frac{1}{l}\int_0^l \left\{ E\left[\left(u(x,t) - \bar{u}(x) \right)^2 \right] \right\}^{1/2} dx \qquad (41)$$

$$\sigma_v = \frac{1}{l}\int_0^l \left\{ E\left[\left(\dot{u}(x,t) \right)^2 \right] \right\}^{1/2} dx \qquad (42)$$

where the overbar indicates the mean value with respect to time and $E[\cdot]$ indicated the expected value. Integration over the cable length reflects how well a particular control approach can reduce the vibration throughout the cable. Herein, other than the two hybrid control cases, three other types of control strategies: optimal passive, active, and ideal semi-active control were also analyzed. Fig. 17 shows the ratio of response performance index for each control case over that of the original uncontrolled case, as the mean wind speed increases from 5 to 30 m/s. For each mean wind speed, the performance indexes were calculated based on 600 seconds of vibration. Figs. 17(a) and 17(b) show the cable displacement and velocity responses, respectively. The optimal passive and active cases are seen to be the upper and lower bounds for these results, respectively. Clearly, the performance of all three semi-active control strategies (hybrid Cases (a) and (b) plus the ideal semi-active) falls between that of the optimal passive and active control. It is seen that the performance of both hybrid control strategies is almost identical to that of optimal passive control when the mean wind speed is less than 10 m/s. This suggests that the energy harvested under such a condition might not be sufficient to sustain the semi-active operation of the damper. As the wind speed exceeds 10 m/s, the effect of the semi-active control strategies starts to be revealed, and the control performance gradually starts to out-perform that of the optimal passive control. Between the two hybrid control cases, it is seen that the performance of Case (a) is always better than that of Case (b), and approaches that of ideal semi-active control as the mean wind speed increases.

To see how much improvement is obtained by utilizing the hybrid control over the optimal passive damper, a reduction parameter r is defined as

$$r = \frac{\sigma_{pas} - \sigma_{hyd}}{\sigma_{pas}} \qquad (43)$$

In this equation, variables with the subscripts "pas" and "hyb" are the response quantities associated with the passive and hybrid control, respectively. The reduction parameters in terms of displacement and velocity responses for both cases are plotted in Fig. 18. It is seen that the damper operating in the hybrid mode is able to provide further response reduction when compared to its passive mode. Between the hybrid Cases (a) and (b), the results show that Case (a) can mitigate more cable vibration. Between the mean wind speeds of 14 and 25 m/s, the average further reductions for the hybrid Case (a) are about 3% and 5.7% for the displacement and velocity responses, respectively, while those for the hybrid Case (b) are about 1.5% and 1% only. It is also seen that the advantage of hybrid control decreases as the mean wind speed exceeds 17 m/s. This could be attributed to the limitation of the damper's force capacity. While the passive force of the damper is linearly proportional to the cable response at the attachment location, its semi-active control force actually is capped by the maximum force f_{max} that is related to its designed stall toque of motor T_{stall}. Hence the effect of semi-active control would reduce when the semi-active control force is saturated at its maximum capacity and cannot gain the full benefit of the optimal control algorithm.
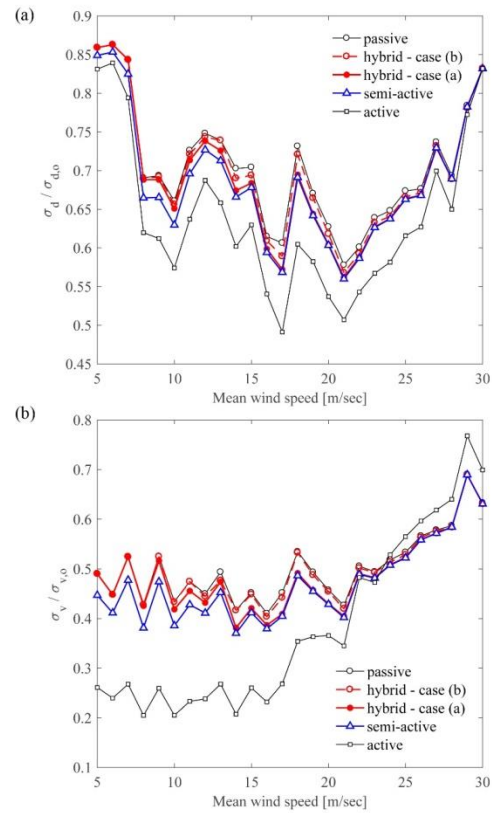

Fig. 17 Comparison of different control methods: (a) displacement, and (b) velocity
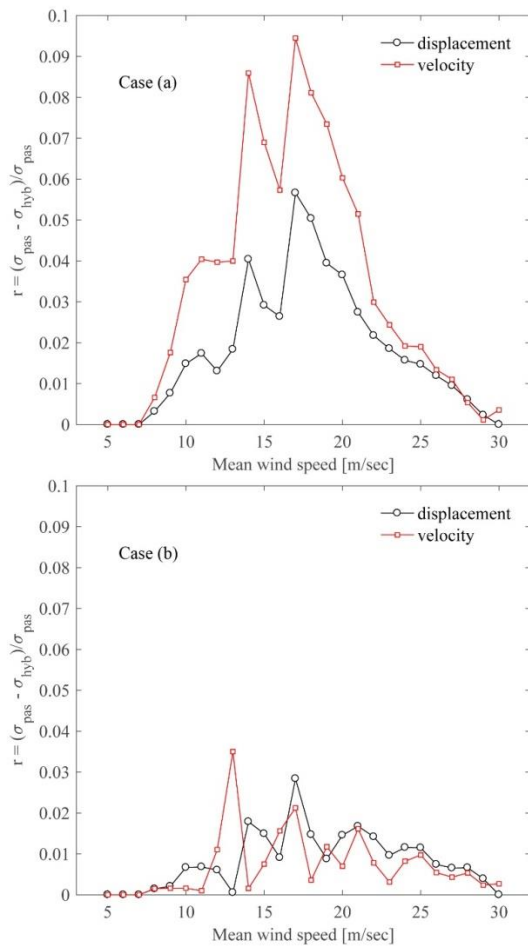
Fig. 18 Performance gain of hybrid control Cases (a) and (b) over optimal passive case
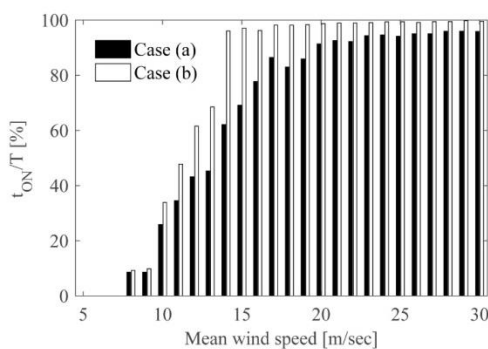

Fig. 19 ON time ratio vs. mean wind speed

Fig. 19 further plots the "on-time" duration for the two hybrid cases. It is seen that when the mean wind speed is below 10 m/s, both cases have a same on-time of about 10%, indicating that the speed of energy harvesting is quite slow. The on-time for the semi-active control increases as the mean wind speed increases. Note that when the mean wind speed exceeds 15 m/s, the on-time for Case (b) is near

100% suggesting that the inflow power is larger than the energy consumed by the semi-active control operation. As for Case (a), its on-time reaches about 80% when the mean wind speed reaches 20 m/s. This indicates that the speed of the inflow energy is quite rapid and can recharge the battery from 20% to 30 % SOC in a very short period of time.

These results show that it is advantageous to decouple the energy harvesting circuit from the semi-active control operation. Harvesting energy during the semi-active control operation appears to be an attractive option but can lead to less satisfactory control performance due to the smaller feasible force-velocity region for the damper. Decoupling these two functions may reduce the energy harvesting period but results in a better control performance.

4. Conclusions

A new self-powered hybrid electromagnetic damper that can harvest energy while mitigating vibration of a structure is presented in this study. The damper can switch between an energy harvesting passive mode and a semi-active mode depending on the amount of energy harvested and stored in the battery. The energy harvested from the vibration is employed to power up the monitoring and electronic components necessary for the semi-active control, which provided the damper with an autonomous hybrid control capability. The device mechanism and circuitry that could realize this self-powered hybrid electromagnetic damper were described in this paper. The proposed hybrid circuit design could offer two possible options for the semi-active control: without energy harvesting and with energy harvesting. Parameters determining the feasible force-velocity regions of the damper for these two options are identified and discussed. The proposed self-powered hybrid electromagnetic damper was evaluated through a numerical simulation on vibration mitigation of an actual bridge stay cable under wind excitation. The results showed that the proposed hybrid damper started to outperform conventional optimal passive dampers when the mean wind speed exceeded 10 m/s. This performance improvement was gained without the need for additional external power. The trade-off between the feasible force-velocity range and the duration of the semi-active control for the example stay cable was investigated. Analysis showed that the damper had a wider feasible force-velocity range when the semi-active control was decoupled from the energy harvesting. Such a characteristic led to better control performance overall although the vibrational energy could not be harvested at all times.

References

Caetano, E.d.S. (2007). *Cable Vibration in Cable-stayed Bridges*, International Association for Bridge and Structural Engineering, Switzerland.

Cahill, P., Nuallain, N.A.N., Jackson, N., Mathewoson, A., Karoumi, R. and Pakrashi, V. (2014), "Energy harvesting from train-induced response in bridges", *J. Bridge Eng.*, **19**(9).

Casciati, F. and Rossi, R. (2007), "A power harvester for wireless sensing applications", *Struct. Control Health Monit.*, **14**(4), 649-659.

Casciati, S., Faravelli, L. and Chen, Z. (2012), "Energy harvesting and power management of wireless sensors for structural control applications in civil engineering", *Smart Struct. Syst.*, **10**(3), 299-312.

Cassidy, I. (2012), "Control of vibratory energy harvesters in the presence of nonlinearities and power-flow constraints", PhD Dissertation, Duke University.

Cassidy, I.L., Scruggs, J.T. and Behrens, S. (2011), "Design of electromagnetic energy harvesters for large-scale structural vibration applications", *Proceedings of SPIE7977*, San Diego, California.

Chen, C. and Liao, W.H. (2012), "A self-sensing magnetorheological damper with power generation", *Smart Mater. Struct.*, **21**(2).

Cho, S.W., Jung, H.J. and Lee, I.W. (2005), "Smart passive system based on magnetorheological damper", *Smart Mater. Struct.*, **14**(4).

Choi, Y.T. and Wereley, N.M. (2009), "Self-powered magnetorheological dampers", *J. Vib. Acoust.*, **131**(4).

Dyke, S.J., Spencer, B.F., Sain, M.K. and Carlson, J.D. (1996), "Modeling and control of magnetorheological dampers for seismic response reduction", *Smart Mater. Struct.*, **5**(5).

Gonzalez-Buelga, A., Clare, L.R., Cammarano, A., Neild, S.A., Burrow, S.G. and Inman, D.J. (2014), "An optimised tuned mass damper/harvester device", *Struct. Control Health Monit.*, **21**(8), 1154-1169.

Gonzalez-Buelga, A., Clare, L.R., Neild, S.A., Burrow, S.G. and Inman, D.J. (2015), "An electromagnetic vibration absorber with harvesting and tuning capabilities", *Struct. Control Health Monit.*, **22**(11), 1359-1372.

Green, P.L., Papatheou, E. and Sims, N.D. (2013), "Energy harvesting from human motion and bridge vibrations: An evaluation of current nonlinear energy harvesting solutions", *J. Intel. Mat. Syst. Str.*, **24**(12), 1494-1505.

Huang, H., Sun, L. and Jiang, X. (2012), "Vibration mitigation of stay cable using optimally tuned MR damper", *Smart Struct. Syst.*, **9**(1), 35-53.

Hui, M.C.H., Larsen, A. and Xiang, H.F. (2009a), "Wind turbulence characteristics study at the Stonecutters Bridge site: Part I—Mean wind and turbulence intensities", *J. Wind Eng. Ind. Aerod.*, **97**(1), 22-36.

Hui, M.C.H., Larsen, A. and Xiang, H.F. (2009b), "Wind turbulence characteristics study at the Stonecutters Bridge site: Part II: Wind power spectra, integral length scales and coherences", *J. Wind Eng. Ind. Aerod.*, **97**(1), 48-59.

Irvine, H.M. (1981), *Cable Structures*, MIT Press, Cambridge, Massachusett, USA.

Johnson, E.A., Baker, G.A., Spencer, B.F. and Fujino, Y. (2007), "Semiactive damping of stay cables", *J. Eng. Mech. - ASCE*, **133**(1), 1-11.

Jung, H.J., Kim, I.H. and Koo, J.H. (2011), "A multi-functional cable-damper system for vibration mitigation, tension estimation and energy harvesting", *Smart Struct. Syst.*, **7**(5), 379-392.

Kim, S.S. and Okada, Y. (2001), "Variable resistance type energy regenerative damper using pulse width modulated step-up chopper", *J. Vib. Acoust.*, **124**(1), 110-115.

Kollmorgen (2016), "AKM Servomotor Selection Guide; Retrieved from www.kollmorgen.com/".

Krenk, S. (2000), "Vibrations of a taut cable with an external damper", *J. Appl. Mech.*, **67**(4), 772-776.

Lefeuvre, E., Audigier, D., Richard, C. and Guyomar, D. (2007), "Buck-boost converter for sensorless power optimization of piezoelectric energy harvester", *IEEE T. Power Electr.*, **22**(5), 2018-2025.

Li, Z., Zuo, L., Luhrs, G., Lin, L. and Qin, Y.X. (2013), "Electromagnetic energy-harvesting shock absorbers: design, modeling, and road tests", *IEEE T. Veh. Technol.*, **62**(3), 1065-1074.

Main, J.A. and Jones, N.P. (2001), "Evaluation of viscous dampers for stay-cable vibration mitigation", *J. Bridge Eng.*, **6**(6), 385-397.

Ottman, G.K., Hofmann, H.F. and Lesieutre, G.A. (2003), "Optimized piezoelectric energy harvesting circuit using step-down converter in discontinuous conduction mode", *IEEE T. Power Electr.*, **18**(2), 696-703.

Pacheco, B.M., Fujino, Y. and Sulekh, A. (1993), "Estimation curve for modal damping in stay cables with viscous damper", *J. Struct. Eng. - ASCE*, **119**(6), 1961-1979.

Pillay, P. and Krishnan, R. (1989), "Modeling, simulation, and analysis of permanent-magnet motor drives. I. The permanent-magnet synchronous motor drive", *IEEE T. Ind. Appl.*, **25**(2), 265-273.

Roshan, Y.M., Maravandi, A. and Moallem, M. (2015), "Power electronics control of an energy regenerative mechatronic damper", *IEEE T. Ind. Electron.*, **62**(5), 3052-3060.

Sarkar, P.K. (2015), *Advanced Process Dynamics and Control*, PHI Learning Private Limited.

Scruggs, J.T. and Iwan, W.D. (2003), "Control of a civil structure using an electric machine with semiactive capability", *J. Struct. Eng. - ASCE*, **129**(7): 951-959.

Shen, W. and Zhu, S. (2015), "Harvesting energy via electromagnetic damper: Application to bridge stay cables", *J. Intel. Mat. Syst. Str.*, **26**(1), 3-19.

Shen, W., Zhu, S. and Xu, Y. (2012), "An experimental study on self-powered vibration control and monitoring system using electromagnetic TMD and wireless sensors", *Sensor Actuat. - A: Physical*, **180**, 166-176.

Shen, W., Zhu, S., Zhu, H. and Xu, Y.I. (2016), "Electromagnetic energy harvesting from structural vibrations during earthquakes", *Smart Struct. Syst.*, **18**(3), 449-470.

Shi, D., Chen, L., Wang, R., Jiang, H. and Shen, Y. (2014), "Design and experiment study of a semi-active energy-regenerative suspension system", *Smart Mater. Struct.*, **24**.

Suda, Y., Nakadai, S. and Nakano, K. (1998), "Hybrid suspension system with skyhook control and energy regeneration (development of self-powered active suspension)", *Vehicle Syst. Dyn.*, **29**, 619-634.

Takeya, K., Sasaki, E. and Kobayashi, Y. (2016), "Design and parametric study on energy harvesting from bridge vibration using tuned dual-mass damper systems", *J. Sound Vib.*, **361**, 50-65.

Tang, X. and Zuo, L. (2012), "Simultaneous energy harvesting and vibration control of structures with tuned mass dampers", *J. Intel. Mat. Syst. Str.*, **23**(18), 2117-2127.

Tremblay, O. and Dessaint, L. (2009), "Experimental validation of a battery dynamic model for EV applications", *World Electric J.*, **3**, 289-298.

von Kármán, T. (1948), "Progress in the statistical theory of turbulence", *Proceedings of the National Academy of Science*.

Yu, Z. and Xu, Y.L. (1998), "Mitigation of three-dimensinal vibration of inclined sag cable using discrete oil dampers — I. formulation", *J. Sound Vib.*, **214**(4), 659-673.

Zhou, Q., Nielsen, S.R.K. and Qu, W.L. (2006), "Semi-active control of three-dimensional vibrations of an inclined sag cable with magnetorheological dampers", *J. Sound Vib.*, **296**(1), 1-22.

Zhu, S., Shen, W. and Xu, Y. (2012), "Linear electromagnetic devices for vibration damping and energy harvesting: Modeling and testing", *Eng. Struct.*, **34**, 198-212.

Zuo, L. and Cui, W. (2013), "Dual-functional energy-harvesting and vibration control: electromagnetic resonant shunt series tuned mass dampers", *J. Vib. Acoust.*, **135**(5).

Zuo, L. and Tang, X. (2013), "Large-scale vibration energy harvesting", *J. Intel. Mat. Syst. Str.*, **24**(11), 1405-1430.

BS